nature communications

Article

https://doi.org/10.1038/s41467-024-55396-3

Structural basis of human VANGL-PRICKLE interaction

Received: 21 June 2024

Accepted: 15 November 2024

Published online: 03 January 2025

Check for updates

Yanyi Song[1,5], Shuyi Jian[2,5], Junlin Teng[2], Pengli Zheng[2,3] ✉ & Zhe Zhang[1,3,4] ✉

Planar cell polarity (PCP) is an evolutionarily conserved process for development and morphogenesis in metazoans. The well-organized polarity pattern in cells is established by the asymmetric distribution of two core protein complexes on opposite sides of the cell membrane. The Van Gogh-like (VANGL)-PRICKLE (PK) pair is one of these two key regulators; however, their structural information and detailed functions have been unclear. Here, we present five cryo-electron microscopy structures of human VANGL1, VANGL2, and their complexes with PK1 at resolutions of 2.2–3.0 Å. Through biochemical and cell imaging experiments, we decipher the molecular details of the VANGL-PK interaction. Furthermore, we reveal that PK1 can target VANGL-containing intracellular vesicles to the peripheral cell membrane. These findings provide a solid foundation to understand the explicit interaction between VANGL and PK while opening new avenues for subsequent studies of the PCP pathway.

Cell polarization plays a vital role in diverse physiological processes within metazoans. Planar cell polarity (PCP; orthogonal to the apical-basal axis) generates asymmetries in both individual cells and cell populations, especially along the anteroposterior axis of the body[1,2]. PCP was originally characterized in *Drosophila* and later proven to be conserved in vertebrates. PCP ensures the alignment of body hair orientation, polarized localization of cilia, and the convergent extension and neurulation during development[3–8]. Considering that polarized cell behaviors are essential for ontogenesis and the physiological functions of various organs, defects in PCP signaling contribute to numerous human diseases, particularly developmental disorders such as neural tube defects (NTDs)[9].

At the molecular level, PCP is mainly established by the asymmetric distribution of two core protein complexes on the opposite sides of a cell. In vertebrates, one complex attaches to the proximal side of the membrane, consisting of the membrane component Vang-like (VANGL) and the cytoplasmic component Prickle (PK). The other complex is localized to the distal side of the membrane, comprising the membrane receptor Frizzled (FZD) and the cytoplasmic proteins Dishevelled (Dsh)-like (DVL) and Inversin (also known as Diego or Dgo). DVL can also interact with VANGL in a competitive manner with PK, a process that is regulated by the post-translational phosphorylation of a specific tyrosine residue within VANGL during the establishment of PCP[10,11]. Furthermore, a common membrane adapter CELSR (also known as Flamingo or Fmi) is also engaged in both of these complexes, likely bridging their intercellular transmembrane interaction and facilitating PCP signaling. The interaction of these two complexes between adjacent cells and their repulsion within the same cell synergistically stabilize and propagate their directional arrangement in a group of cells, thereby maintaining the polarity pattern integrity and establishing well-organized spatial information at the tissue and organ levels[1,12–14]. Thus far, upstream and downstream signals in the PCP pathway are not well understood. However, it is widely accepted that the molecular gradients of specific WNT ligands (e.g., WNT5A, WNT7A, and WNT11) provide guidance for PCP formation[15–22]. Moreover, the known downstream effectors of PCP are closely associated with cytoskeletal rearrangement and nuclear signaling components,

[1]State Key Laboratory of Membrane Biology, Peking University-Tsinghua University-National Institute of Biological Sciences Joint Graduate Program, Academy for Advanced Interdisciplinary Studies, Peking University, Beijing, China. [2]MOE Key Laboratory of Cell Proliferation and Differentiation, School of Life Sciences, Peking University, Beijing, China. [3]Center for Life Sciences, Academy for Advanced Interdisciplinary Studies, Peking University, Beijing, China. [4]School of Life Sciences, Peking University, Beijing, China. [5]These authors contributed equally: Yanyi Song, Shuyi Jian. ✉e-mail: zhengpl@pku.edu.cn; zzhang01@pku.edu.cn

including Rho family small GTPases, Rho-associated kinase (ROK), myosin II, and the Jun N-terminal kinase (JNK) pathway[23–28].

Vang, the abbreviation for "Van Gogh", is also known as Strabismus (Stbm)[29]. Whereas *Drosophila* only has one Vang protein, vertebrates contain two paralogs (VANGL1 and VANGL2); these paralogs share more than 70% sequence identity in humans. The conserved function of VANGL in PCP generation has been confirmed within various species[29–34]. Notably, the two VANGL counterparts synergistically control the PCP process. Although VANGL2 alterations can cause more severe developmental defects than VANGL1 alterations, the difference is most likely related to their distinct spatiotemporal expression patterns[35]. Accordingly, mutations in both *VANGL* genes have been discovered in human NTD patients[36,37]. Furthermore, *Drosophila* Prickle and its four vertebrate paralogs (Prickle-like protein 1-4, or PK1-PK4) are reportedly associated with PCP[38–43]. Specifically, they mediate PCP signaling by assembling into a complex with VANGL and antagonizing the localization of DVL around the VANGL/PK-enriched membrane area[41,44,45]. Although VANGL-PK is one of the two core protein regulators in PCP, the overall architecture of VANGL and its detailed interactions with PK remain unclear, greatly hindering the overall understanding of this signaling pathway.

Here, we report the cryo-electron microscopy (cryo-EM) structures of human VANGL1 and VANGL2, as well as their complex structures with PK1. We also analyzed their interactions with both biochemical and cell imaging experiments. Taken together, our work reveals the molecular details of the VANGL-PK interaction and provides insights regarding their functional connection.

Results

Architecture of the VANGL hexamer

We expressed the full-length (FL) human VANGL1 and VANGL2 in HEK293S cells, then purified these two proteins using detergent lauryl maltose neopentyl glycol (LMNG) and cholesteryl hemisuccinate (CHS). Their gel filtration peaks indicate that VANGL exists as an oligomer (the molecular weight of the monomer is ~60 kDa) (Supplementary Fig. 1a). To clarify the oligomerization status, we performed analytical ultracentrifugation (AUC) analyses; the results showed that the molecular weight of the VANGL oligomers approximately matched the hexamer size, with only a minor portion of trimers being present (Supplementary Fig. 1b). Next, we determined the cryo-EM structures of VANGL1 and VANGL2 to resolutions of 3.0 Å and 2.9 Å, respectively (Fig. 1a, and Supplementary Figs. 1 and 2, and Table 1). These two structures were very similar, as demonstrated by the overall root-mean-square deviation (RMSD) of 1.9 Å (Fig. 1b and Supplementary Fig. 3a). Consistent with the gel filtration and AUC results (Supplementary Fig. 1a, b), in these structures, both VANGL1 and VANGL2 were organized as dimers of trimers, forming hexamers with D3 symmetry (Fig. 1a, b). Notably, the two trimers directly faced each other through their cytoplasmic portions; thus, the transmembrane regions were placed on the lateral sides, resulting in a rod-like hexamer with an overall length of approximately 210 Å (Fig. 1b). Importantly, the N-terminal regions preceding the transmembrane domain of VANGL ($VANGL1^{1\text{-}113}$ and $VANGL2^{1\text{-}108}$) were not visible in our EM maps (Fig. 1a), suggesting that they are flexible and not involved in the construction of the VANGL core structure.

VANGL can be roughly divided into five domains: the N-terminal domain (NTD), transmembrane domain (TMD), juxtamembrane domain (JMD), helical bundle domain (HBD), and C-terminal domain (CTD) (Fig. 1c–e and Supplementary Fig. 3b). Intriguingly, the HBD ($VANGL1^{292\text{-}445}$ and $VANGL1^{288\text{-}442}$), which consists of six helices (α2-α7), is inserted between the two halves of the JMD (Fig. 1c–e and Supplementary Fig. 3b). Surprisingly, the α2 helix was not resolved in the VANGL2 structure, suggesting that this helix has greater mobility (Supplementary Fig. 3b). The JMD mainly consists of five antiparallel β-strands and one α-helix (Fig. 1c–e and Supplementary Fig. 3b), primarily resembling the structure of the anti-CRISPR protein AcrIE3 (PDB: 7CHQ)[46] based on DALI server analysis (a Z-score of 4.6)[47] (Supplementary Fig. 3c). The assembly of the VANGL trimer is mediated by three tiers of inter-subunit interactions (Fig. 1e and Supplementary Fig. 3b). In the top layer, the TMDs are tightly packed together via TM2-TM4 (Fig. 1f and Supplementary Fig. 3d). In the middle layer, the JMDs are clustered immediately beneath the membrane. In the bottom layer, the HBDs mutually bind to form a triangular base (Fig. 1g and Supplementary Fig. 3e). Notably, the HBDs also interact with the adjacent JMD to further stabilize the trimer (Fig. 1e and Supplementary Fig. 3b). Additionally, the CTDs extend outward in loop form to tie the three subunits together, passing through the TMD-JMD interface of one neighboring subunit and finally inserting within the α4-α5 loop of the HBD in the third subunit (Fig. 1e and Supplementary Fig. 3b). In this manner, the structure of the trimer becomes particularly robust. Subsequent dimerization of the VANGL trimer is mainly mediated by several residues in the α4 helix of HBD on the bottom layer of the cytoplasmic region, including His340, Glu342, Tyr345, Glu346, and Glu349 in VANGL1 or His338, Glu340, Tyr343, Glu344, and Glu347 in VANGL2 (Fig. 1h and Supplementary Fig. 3f). Furthermore, we predicted the structures of the VANGL trimer and hexamer using AlphaFold3[48]. The predicted trimer structure aligns well with our determined structure, with an RMSD of about 1.0 Å (Supplementary Fig. 4a, b). However, the modeled hexamer structure envisioned as two adjacent trimers does not align with the structure we resolved (Supplementary Fig. 4c).

Structure determination of the VANGL1-PK1 complex

To gain further insights regarding the interaction between VANGL and PK1, we sought to determine the structure of their complex. Because the FL human PK1 tended to aggregate during purification, we attached a maltose-binding protein (MBP) tag to its C-terminus and co-expressed it with VANGL to achieve greater solubility. Eventually, compared with VANGL2, VANGL1 was able to form a more stable complex with PK1. However, even in the VANGL1-PK1 complex, the proportion of PK1 appeared low (Supplementary Fig. 5a), indicating that PK1-VANGL1-binding is relatively weak or that the stoichiometric ratio is less than 1:1. Nevertheless, we solved the cryo-EM structure of this VANGL1-PK1 complex at a resolution of 2.6 Å (Fig. 2a, and Supplementary Fig. 5 and Table 1). Upon binding to PK1, VANGL1 maintained its hexamer structure, similar to its unbound form, but the two trimers were compressed by approximately 3 Å along their long axis (Fig. 2b). Upon closer inspection, we discovered a cluster of greater densities near the VANGL1 trimer-trimer interface (Fig. 2c). Thus, we presumed that these densities most likely originated from PK1 and that PK1 binding influenced the structure of VANGL1. Nevertheless, it remains possible that these densities could arise from other unresolved regions of VANGL1, such as the N-terminal domain. When we conducted three-dimensional (3D) reconstruction with C1 symmetry (rather than C3 or D3 symmetry), we found that the shapes, sizes, and strengths of the additional densities associated with each VANGL1 subunit were distinct (Supplementary Fig. 6); these results suggested that PK1 could not bind in a comparable manner to each VANGL1 subunit and/or that the bound PK1 was flexible, consistent with our findings in protein purification (Supplementary Fig. 5a).

Characterization of specific regions of VANGL and PK1 involved in their interaction

PK1 is attached to the highly positively charged surface of VANGL1, which is formed by multiple arginine and lysine residues in the α3-α5 helices of the HBD, including Arg334, Arg352, Arg353, Lys355, Lys356, Arg357, Arg360, Arg403, Lys407, and Arg410 (Fig. 2d, e). Thus, we hypothesized that PK1 could utilize a negatively charged area to bind VANGL through electrostatic interactions. The VANGL-binding region of PK is reportedly located in its C-terminus[44], which contains a large

https://doi.org/10.1038/s41467-024-55396-3

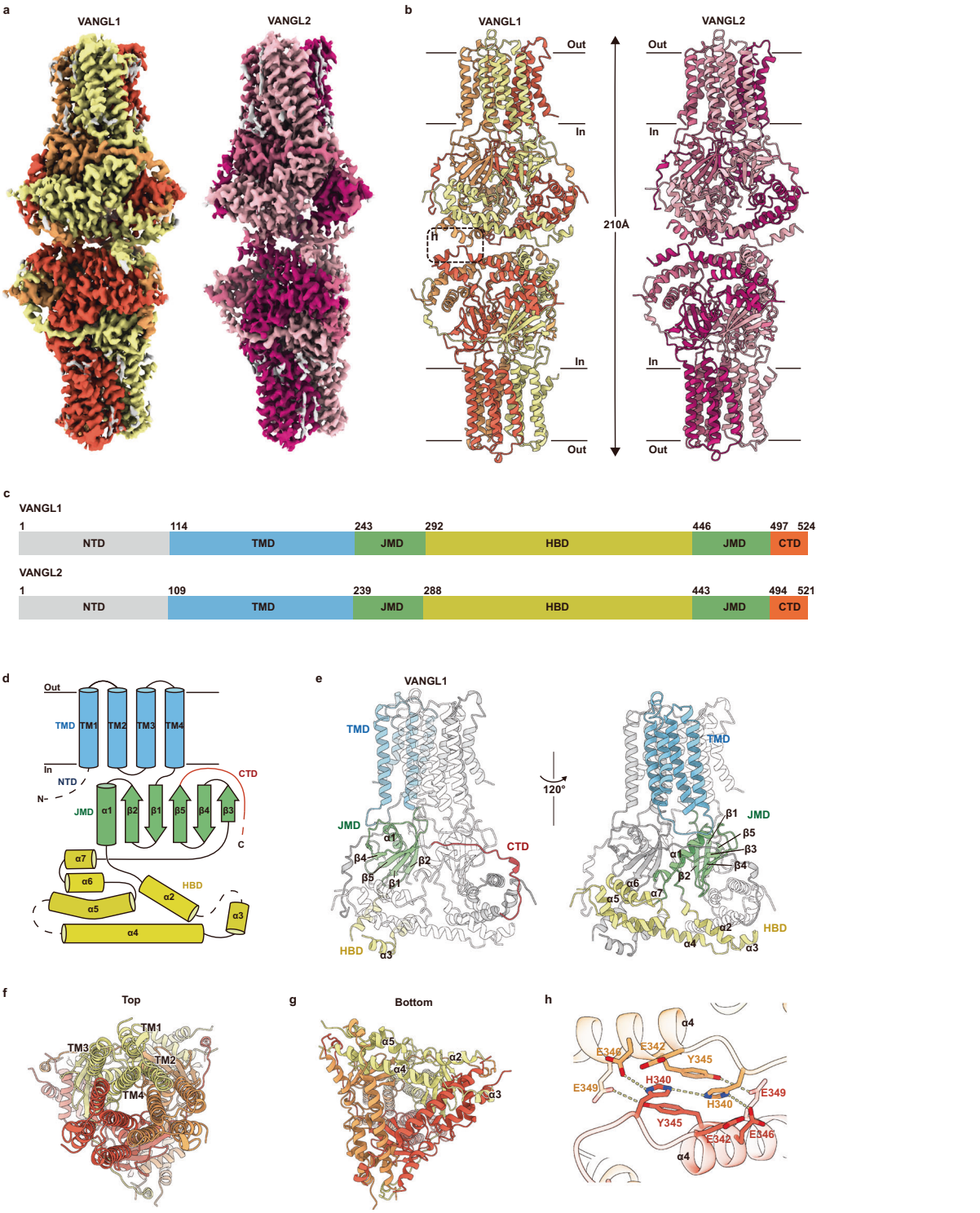

Fig. 1 | Cryo-EM structures of the VANGL1 and VANGL2 hexamer. a Cryo-EM maps of the VANGL1 (left) and VANGL2 (right) hexamers. Maps are reconstructed using D3 symmetry and colored by chains. Extra scattered densities around the transmembrane regions are colored in grey, which might be lipids or detergents. The contour levels of these sharpened maps are 0.47 (VANGL1) and 0.16 (VANGL2), respectively. **b** Cartoon representations of the VANGL1 (left) and VANGL2 (right) structures. **c** The domain composition within the primary structures of VANGL1 and VANGL2. **d** Topology diagram of the VANGL protein. The TMD, JMD, HBD, and CTD are represented in blue, green, yellow, and red, respectively. The invisible NTD is indicated with dashed line. **e** Assembly of the VANGL1 trimer. One VANGL subunit is colored by different domains. The color code is the same as that in **c**. The other two subunits are colored in white and grey, respectively. Top (**f**) and bottom (**g**) views of the VANGL1 trimer. **h** Interaction details between two VANGL1 trimers for their hexamer assembly as indicated in the insets of (**b**). Residues involved in their interaction are shown with side chains. Dashed lines represent hydrogen bond interactions (<4.0 Å).

https://doi.org/10.1038/s41467-024-55396-3

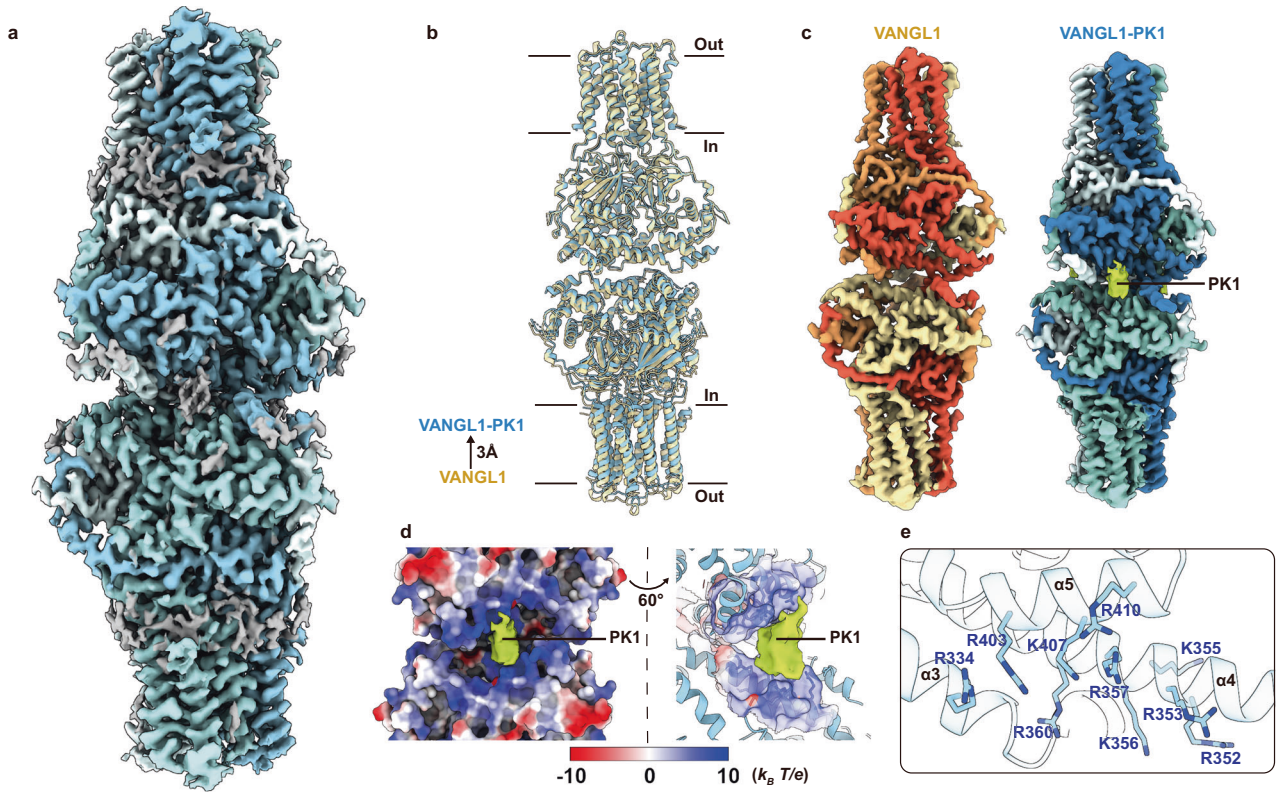

Fig. 2 | Cryo-EM structure of the VANGL1-PK1 complex. a Cryo-EM map of the VANGL1-PK1 complex. The sharpened map is reconstructed with D3 symmetry shown at a contour level of 0.105. The VANGL1 densities are colored in blue and the extra densities are colored in grey. **b** Superposition of individual VANGL1 and the VANGL1-PK1 complex structures based on the top VANGL1 trimer. **c** Unsharpened cryo-EM maps of VANGL1 and the VANGL1-PK1 complex refined with C3 symmetry. Maps are colored by chains and the potential PK1 densities are colored in green. The contour levels of these maps are 0.350 (VANGL1) and 0.075 (VANGL1-PK1), respectively. **d** Surface electrostatic potential (in units of k_BT/e, where k_B is the Boltzmann constant, T is the absolute temperature and e is the elementary charge) of the VANGL1 trimer-trimer interface that interacts with PK1. **e** The ten positively charged residues on the potential PK1-binding interface of VANGL1 are shown with side chains.

quantity of negatively charged residues (Fig. 3a). Moreover, according to AlphaFold prediction[48], the C-terminus of PK1 is disordered without any secondary structure features. These analyses further indicate that the weak densities of PK1 observed in the VANGL1-PK1 EM map (Fig. 2c and Supplementary Fig. 6) may originate from its C-terminus.

To better identify the specific regions of VANGL1 and PK1 involved in their interaction, we conducted pull-down experiments. We mutated 10 positively charged residues in the HBD of VANGL1 that are located near the potential PK1 binding site to alanine (VANGL1^{10mut}); we also prepared several C-terminal truncated constructs of PK1. After these VANGL1 and PK1 variants had been co-expressed in HEK293S cells, we used anti-mCherry nanobody-conjugated resins to capture the mCherry-tagged PK1 protein. By comparing the amount of co-purified GFP-VANGL1, we were able to estimate the binding affinity between the two proteins. Our results showed that VANGL1^{10mut} did not bind PK1 (Fig. 3b and Supplementary Fig. 7a), suggesting that the positively charged surface of VANGL1 is essential for recognition of PK1. Additionally, C-terminal residues 745-790 in PK1 constituted a key region involved in VANGL1-binding because their deletion (PK1$^{\Delta 745\text{-}790}$) nearly abolished the VANGL1-PK1 interaction (Fig. 3c and Supplementary Fig. 7b). To confirm that these 46 residues in PK1 (PK1$^{745\text{-}790}$) are essential for binding to VANGL1, we examined the VANGL1-PK1 interaction solely using PK1 C-terminal peptides. Indeed, these results further supported our conclusion (Fig. 3d and Supplementary Fig. 7c).

Within the VANGL1-binding region of PK1 (PK1$^{745\text{-}790}$), there are two negative-charge concentrated areas: ^{757}EDDD^{760} and ^{771}DSEEE^{775}. Considering that PK1$^{1\text{-}760}$ exhibits almost no VANGL1-binding ability (Fig. 3c and Supplementary Fig. 7b), we inferred that ^{771}DSEEE^{775} in PK1 might be more important for the identification of VANGL1. Thus, we mutated the four negatively charged residues within this region to alanine (DEEE to A) and examined the effect on VANGL1 interaction. Pull-down experiments demonstrated that FL PK1 possessing this substitution could no longer bind VANGL1 (Fig. 3e and Supplementary Fig. 7d). This result clarified the specific residues in PK1 responsible for VANGL1 recognition. Interestingly, PK1$^{761\text{-}790}$ exhibited slightly lower affinity for VANGL1 compared with PK1$^{745\text{-}790}$ (Fig. 3d and Supplementary Fig. 7c). Additionally, mutation of ^{757}EDDD^{760} to alanine (EDDD to A) also weakened the VANGL1-binding affinity of PK1 (Fig. 3e and Supplementary Fig. 7d). Therefore, the first patch of negatively charged region (^{757}EDDD^{760}) might serve as an auxiliary component in the VANGL1 interaction. Because the PK1-binding region is strictly conserved between the two VANGL paralogs (Supplementary Fig. 8a), we speculated that VANGL2 identifies PK1 in the same manner. Indeed, our pull-down results validated this general recognition mechanism (Fig. 3e–g and Supplementary Fig. 7d–f). Of note, a previous study identified a C-terminal fragment of Pk1, corresponding to residues 628-767 of human PK1, as being responsible for Vang binding in *Drosophilia*[44]. This region encompasses the first negatively charged patch (^{757}EDDD^{760}) and is partially consistent with our findings.

Next, to improve the EM densities of the PK1 portion in the VANGL-PK1 complex, we saturated VANGL1 or VANGL2 with the PK1$^{745\text{-}790}$ peptide by incubation at a 1:4 ratio before preparing the cryo-EM samples. Finally, the resolutions of the VANGL1-PK1$^{745\text{-}790}$ and VANGL2-PK1$^{745\text{-}790}$ complex structures were improved to 2.2 Å and 2.5 Å, respectively (Fig. 3h, and Supplementary Figs. 9, 10 and Table 2). In

https://doi.org/10.1038/s41467-024-55396-3

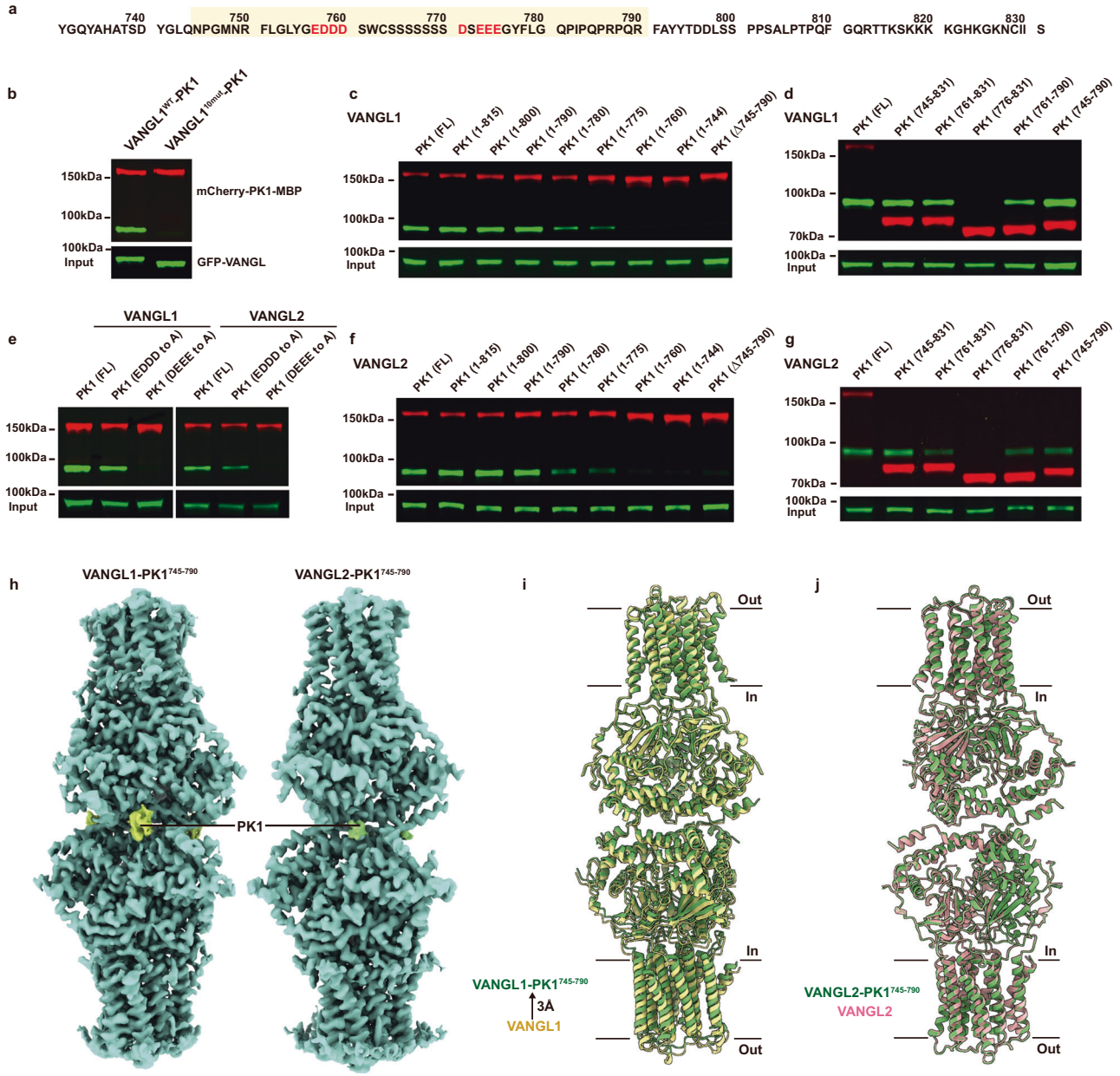

Fig. 3 | Characterization of the specific regions of VANGL and PK1 involved in their interaction. a The C-terminal sequence of PK1. Residues 745–790 are indicated with a yellow box. The two negative charge concentrated areas are marked in red. **b** Pull-down assay to verify the ten positively charged residues of VANGL1 are the key PK1 binding site. Mutation of the ten residues depicted in Fig. 2e to alanine resulted in a complete loss of PK1 binding capability. **c**, **d** Pull-down assay to pinpoint the key regions of PK1 for VANGL1-binding. The VANGL1-PK1 interaction was retained up until the 1–790 truncation variant, but it was gradually reduced in the 1–780 truncation variant and completely lost in the 1–760 truncation variant. Moreover, deletion of the C-terminal residues 745-790 of PK1 (Δ745-790) nearly abolished its binding to VANGL1 (**c**). In the complementation experiments, the C-terminal residues 745-790 of PK1 largely restored its binding ability to VANGL1 (**d**). **e** Pull-down assay to verify the significance of the two negatively charged pieces (^{757}EDDD^{760} and ^{771}DSEEE^{775}) of PK1 in identifying VANGL1. **f**, **g** Pull-down assay to pinpoint the key regions of PK1 for VANGL2 binding. The results were consistent with those observed in (**c**) and (**d**). All experiments in (**c**–**g**) were performed in triplicate with similar results. **h** Cryo-EM maps of the VANGL1-PK1$^{745\text{-}790}$ and VANGL2-PK1$^{745\text{-}790}$ complexes, shown at the contour levels of 0.070 and 0.064, respectively. The densities of PK1 are colored in green. **i** Superposition of VANGL1 (yellow) and the VANGL1-PK1$^{745\text{-}790}$ (green) complex structures. **j** Superposition of VANGL2 (pink) and the VANGL2-PK1$^{745\text{-}790}$ (green) complex structures. The RMSD between VANGL2 and VANGL2-PK1$^{745\text{-}790}$ is 0.38 Å. Source data are provided as a Source Data file.

these maps, the PK1 densities appeared in the same location as in the VANGL1-PK1 complex, confirming that PK1$^{745\text{-}790}$ directs specific binding to VANGL (Fig. 3h). The PK1 densities were relatively weaker in complex with VANGL2 (Fig. 3h) and did not induce the same compression of the VANGL2 hexamer as occurred with VANGL1 in the VANGL1-PK1/PK1$^{745\text{-}790}$ complexes (Figs. 2b and 3i, j). These observations indicated that PK1 has lower affinity for VANGL2 than for VANGL1, consistent with our previous results concerning isolation of the VANGL1-PK1 but not the VANGL2-PK1 complex. Unfortunately, the EM densities of PK1 in these maps remained insufficient to confidently resolve the protein sequence (Fig. 3h). To address this, we further utilized AlphaFold3 to model the VANGL-PK1 and VANGL-PK1$^{745\text{-}790}$ complexes (Supplementary Fig. 4d–g). The modeled complexes revealed that PK1 indeed binds to the positively charged surface of VANGL, employing the same set of negatively charged residues we proposed. Collectively, our structural evidence, pull-down results and

AlphaFold3 modeling substantiated the VANGL-PK1 recognition mechanism.

Based on the findings thus far, we inferred that the specific recognition between VANGL and PK1 is mediated by the electrostatic attraction within a defined region of these proteins. This notion is supported by the high conservation of charged residues mediating their interaction across different species (Supplementary Fig. 8b, c). Moreover, among the four PK paralogs in vertebrates, only PK1 and PK2 synergistically function with VANGL to regulate PCP[41,42]; the functions of PK3 and PK4 are not well understood[38]. Intriguingly, whereas both PK1 and PK2 possess the two pieces of negatively charged sequences for VANGL association, PK3 and PK4 only possess the major sequences (Supplementary Fig. 8d). These results imply that PK3 and PK4 can also bind VANGL but with lower affinity. Their roles in PCP require further investigation.

PK1 helps VANGL-containing vesicles dock to the plasma membrane in a polarized manner

Within the VANGL-PK complex, VANGL is the integral membrane component, whereas PK is the cytoplasmic element. Thus, it is reasonable to conclude that VANGL is responsible for recruiting PK to the plasma membrane before fulfilling its downstream functions[42,44]. We first sought to elucidate the intracellular localization of VANGL1 and VANGL2. However, overexpressed mNeongreen-tagged VANGL1 and VANGL2 proteins were predominantly localized to vesicle-like structures clustered in perinuclear regions, with limited presence at the cell periphery (Fig. 4a). Upon co-labeling with the lysosomal and late endosomal markers Lamp1 and Rab7, respectively, we observed that most VANGL1- and VANGL2-positive puncta were colocalized with lysosomes and late endosomes (Fig. 4a and Supplementary Fig. 11a, b). Additionally, the minor peripheral VANGL1 and VANGL2 signals were consistent with the location of the plasma membrane marker WGA (Supplementary Fig. 11c), suggesting that subsets of VANGL1 and VANGL2 proteins were present on the cell membrane.

Intriguingly, upon co-expression with PK1, most VANGL1- and VANGL2-positive puncta exhibited prominent accumulation near the plasma membrane, especially at the cell leading edge (Fig. 4b–e). C-terminally truncated VANGL1 ($VANGL1^{1\text{-}495}$), which lacks oligomerization ability (Supplementary Fig. 11d), did not accumulate at the cell periphery regardless of PK1 co-expression (Fig. 4d, f). A PK1 variant lacking the VANGL-binding region ($PK1^{1\text{-}744}$) was also dysfunctional (Fig. 4d, e, and g). These data suggest that PK1 is passively recruited by VANGL and actively aids the asymmetric positioning of VANGL by facilitating vesicle docking to the plasma membrane. Surprisingly, $VANGL1^{10mut}$ itself was mostly localized to the plasma membrane with minimal retention in intracellular vesicles, but its distribution was not polarized to the leading edge (Fig. 4d, h). Upon co-expression with PK1, its plasma membrane localization remained unaffected (Fig. 4d, i). Notably, the $VANGL1^{10mut}$ formed trimers instead of hexamers (Supplementary Fig. 11e, f), indicating that these mutations impede the dimerization of VANGL1 trimers, beyond just disrupting PK1 binding. These findings suggest that the positively charged residues in VANGL1 are essential for its hexameric assembly and vesicular localization, in addition to their role in attracting PK1.

To gain further insights regarding the characteristics of the VANGL-PK1-containing vesicles, we performed paxillin immunostaining to label focal adhesions[49]. As expected, vesicles containing VANGL and PK1 were positioned adjacent to, but distinct from, focal adhesions (Fig. 5a). We then used polar-SIM to acquire 3D super-resolution images of these vesicles[50]; the results showed that the vesicles were docked at the bottom plasma membrane of cells (Fig. 5b). Considering the pivotal role of Rab family small GTPases in regulating intracellular vesicle identities and dynamics[51], we proceeded to explore whether specific Rab proteins localize on these VANGL-PK1 vesicles. Because overexpression of PK1 itself resulted in some accumulation near the plasma membrane (Supplementary Fig. 12), likely due to the association with endogenous VANGL proteins, we co-expressed PK1 together with several Rab proteins in U2OS cells to determine their localization. Among the 18 Rab proteins we examined, Rab36 exhibited complete colocalization with PK1-positive vesicles, whereas Rab15 displayed partial colocalization (Fig. 5c, d and Supplementary Fig. 12). Collectively, these findings suggest that the VANGL-PK1 complex orchestrates the polarized accumulation of Rab36- and Rab15-positive vesicles adjacent to the plasma membrane (Fig. 5e). However, further investigation in polarized cells is necessary to confirm the PK1-mediated membrane recruitment of VANGL-containing vesicles and to elucidate the underlying mechanism.

Structural interpretation of the loss-of-function or disease-related mutations in VANGL

Since the identification of loop-tail mutations in Vangl2 (D255E and S464N) in mice in 2001, many missense mutations of VANGL1 and VANGL2 have been successively reported in human patients, especially those can result in NTDs[34,36,37,52–54]. To gain a better mechanistic understanding of these mutations, we mapped them onto the structures of the two VANGL proteins (Fig. 6 and Supplementary Table 3). Overall, we found that the mutations are widely distributed in each domain. Among them, many mutations are located at the timer interface, including Arg181, Val239, Ala404 and Arg517 in VANGL1 and Arg177, Leu242, Thr247, Asp255, Arg353 and Ser464 in VANGL2 (Fig. 6a, e). Therefore, these mutations likely impair VANGL function by interfering with trimer assembly. Additionally, some alterations clearly affect the local structure of individual VANGL subunits. For example, a conserved arginine residue in the JMD (Arg274 in VANGL1 or Arg270 in VANGL2) is essential to maintain the TMD and JMD in close proximity (Fig. 6b, f). Mutation of this residue to either glutamine in VANGL1 (R274Q) or histidine in VANGL2 (R270H) would potentially disrupt its interaction with the TMD. Similarly, the F440V mutation in VANGL1 or F437S mutation in VANGL2 might disturb the internal hydrophobic core of the HBD (Fig. 6c, g). In other cases, hydrophobic residues outside of the TMD are replaced by polar residues, such as mutations F153S and I136N in VANGL1 (Fig. 6d). These changes very likely reduce VANGL stability in the hydrophobic membrane environment or diminish its membrane localization. In summary, our structural findings provide a new foundation to understand the pathogenic mechanisms involving VANGL mutations. Nonetheless, additional biochemical analyses and animal model studies are imperative to confirm the actual impact and clinical significance of these mutations.

Discussion

In this work, we first described the cryo-EM structures of human VANGL1 and VANGL2 hexamers, then analyzed their interactions with PK1 using structural, biochemical, and cell imaging experiments. Finally, we revealed that VANGL and PK1 interact with each other mainly through electrostatic attraction; we characterized the principal charged residues that participate in the interaction between these two proteins. Furthermore, we discovered that PK1 can promote the asymmetric distribution of VANGL to the peripheral or leading edge of the cell membrane via vesicular transport.

This study showed that VANGL and PK did not form a structurally stable complex. Interestingly, the C-terminal 500 residues in PK are intrinsically disordered, including the VANGL-binding regions[48]. This highly flexible structure of PK might be essential for its functional promiscuity, such as interactions with multiple protein partners like VANGL, DVL, INVERSIN, and RICTOR[10,38,40,41,44,55,56]. Similarly, the positively charged surface on the HBD of VANGL ($VANGL1^{334\text{-}410}$ or $VANGL2^{332\text{-}407}$) might also be able to associate with other proteins, some of which may regulate its intracellular trafficking in a manner identical to PK1. These interactions could explain why $VANGL1^{10mut}$ behaves differently from the wild-type protein (Fig. 4b, d, and h). In

https://doi.org/10.1038/s41467-024-55396-3

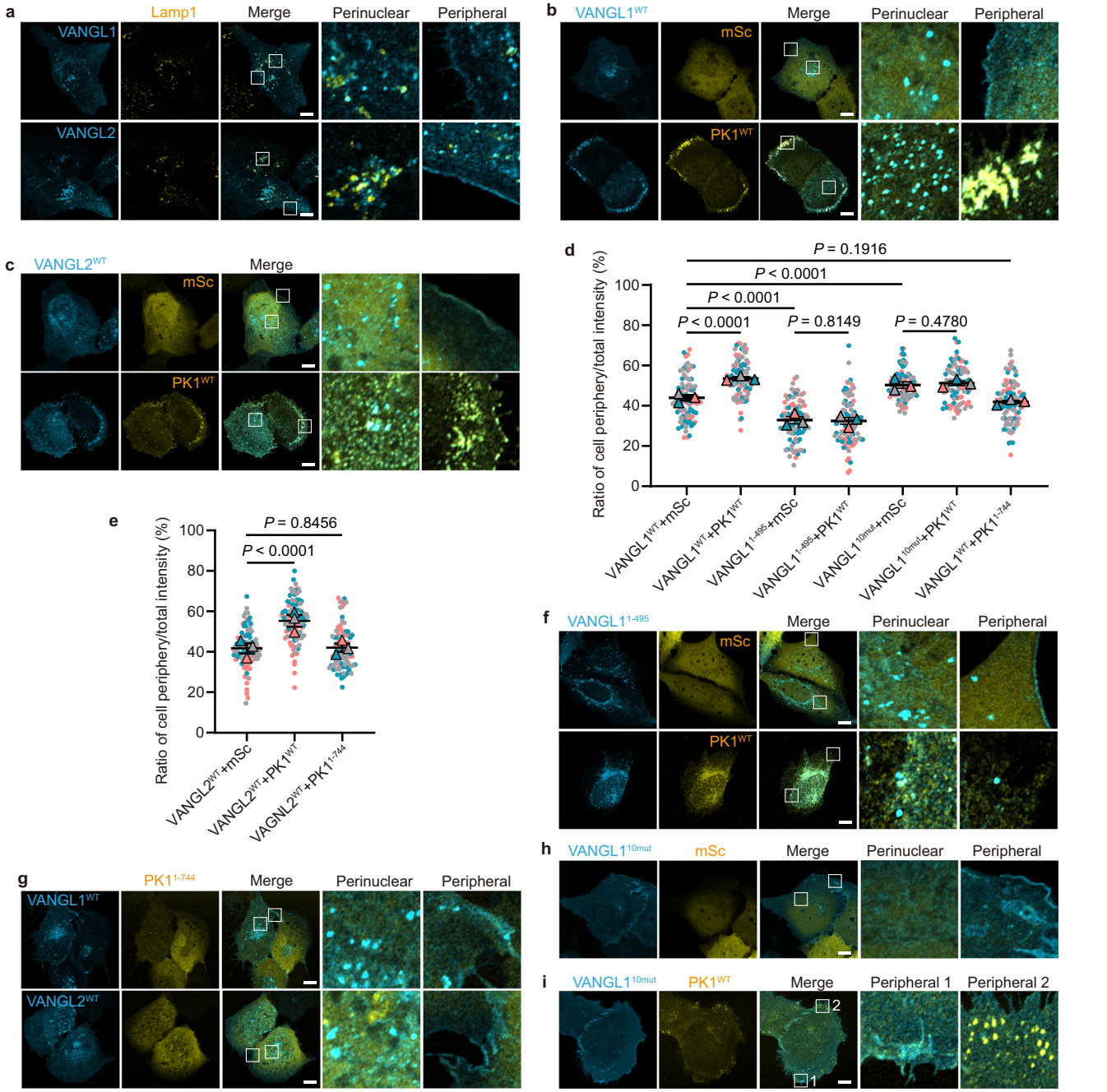

Fig. 4 | The subcellular localization of VANGL1 and VANGL2. a Representative images of U2OS cells co-expressing mNeongreen (mN)-VANGL1/mN-VANGL2 (Cyan) and Lamp1-mApple (Yellow). The experiments were performed in triplicate with similar results. Perinuclear and peripheral regions (outlined) are enlarged on the right. Representative images of U2OS cells co-expressing mN-VANGL1^{WT} (**b**) or mN-VANGL2 ^{WT} (**c**) and mScarlet (mSc) or mSc-PK1^{WT}. **d** Quantifications of the ratio of cell periphery/total intensity (%) for VANGL1 signals in U2OS cells expressing the indicated constructs. **e** Quantifications of the ratio of cell periphery/total intensity (%) for VANGL2 signals in U2OS cells expressing the indicated constructs. The experiments in (**d**) and (**e**) were repeated three times independently, each with n = 30 cells. The data are shown as the mean ± sem, and a two-tailed unpaired Student's t-test was used for statistical analysis. **f** Representative images of U2OS cells co-expressing mN-VANGL1$^{1-495}$ and mSc/mSc-PK1^{WT}. **g** Representative images of U2OS cells co-expressing mN-VANGL1^{WT}/mN-VANGL2^{WT} and mSc-PK1$^{1-744}$. Representative images of U2OS cells co-expressing mN-VANGL1^{10mut} and mSc (**h**) /mSc-PK1^{WT} (**i**). Scale bars in (**a**–**c**) and (**f**–**i**): 10 μm. Source data are provided as a Source Data file.

particular, the VCP-interaction motif (VIM) (RX_5AAX_2R, VANGL1$^{326-336}$ or VANGL2$^{324-334}$), which is near the PK1-binding site, can target VANGL to the endoplasmic reticulum-associated degradation (ERAD) pathway via direct binding to p97/VCP[57].

A recent study has pinpointed a specific region within the Vang/Vangl proteins—residues 302-324 of human VANGL1, residues 298-322 of human VANGL2, and residues 364-387 of *Drosophila* Vangl—as critical for binding both PK and DVL[11]. Interestingly, this region was almost invisible in our structural models and is situated upstream of the binding sites we identified. These findings imply that multiple areas of VANGL may be involved in PK1 binding, highlighting the intricate nature of the VANGL-PK interaction. In terms of the stoichiometry of the VANGL-PK1 interaction, our structural data does not allow us to determine an exact binding ratio due to the ambiguous PK densities. Given that VANGL forms a symmetric hexamer, with PK1-binding sites that are also symmetrical, we speculate that a single VANGL hexamer

https://doi.org/10.1038/s41467-024-55396-3

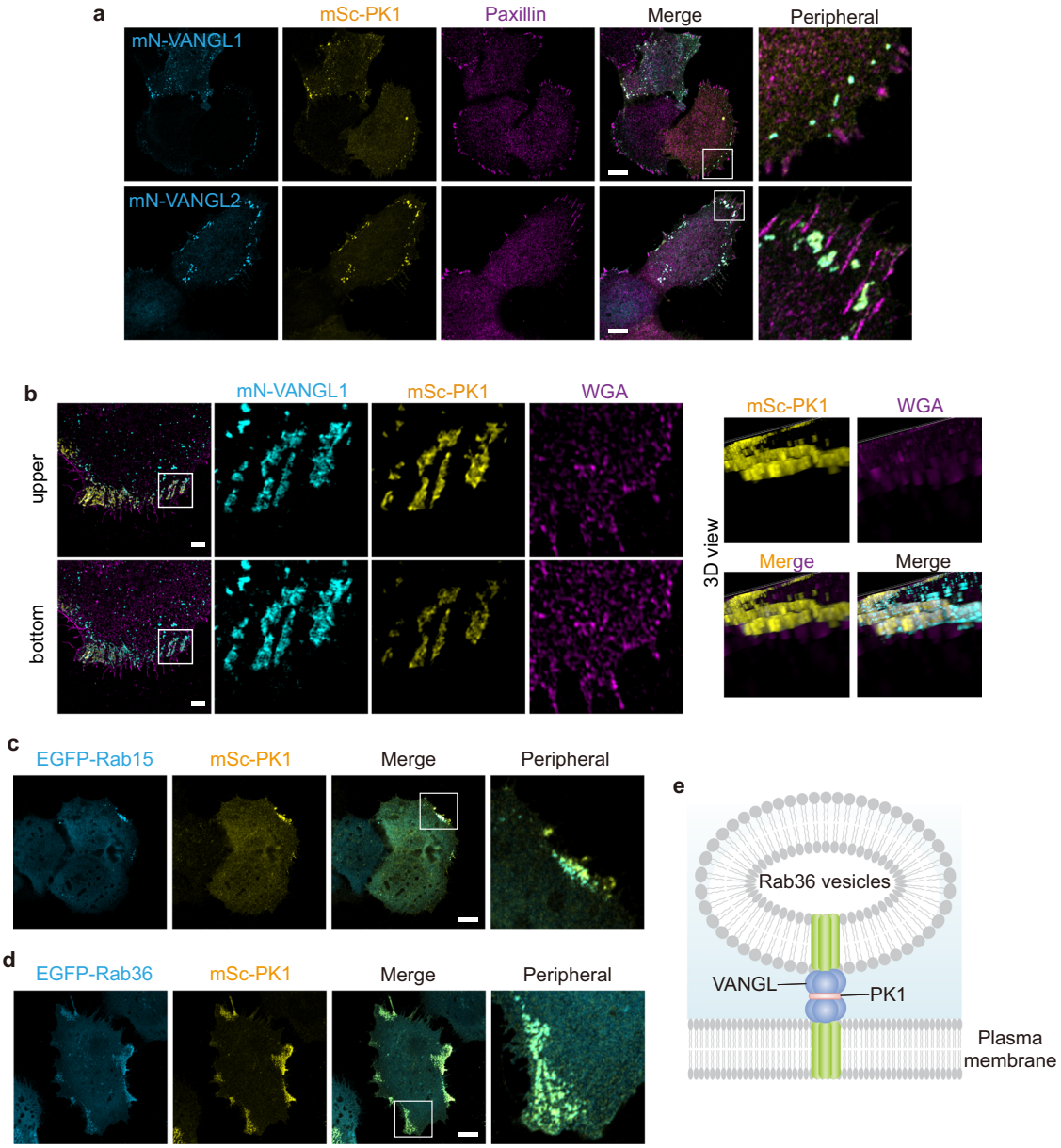

Fig. 5 | Characterization of the VANGL-PK1 containing vesicles. a Representative images of U2OS cells co-expressing mN-VANGL1/VANGL2 (Cyan) and mSc-PK1 (Yellow) which are also immune-stained with anti-Paxillin (Magenta). Peripheral regions (outlined) are enlarged on the right. Scale bars: 10 μm. **b** Representative polar-SIM images of U2OS cells co-expressing mN-VANGL1 (Cyan) and mSc-PK1 (Yellow) which are also stained with WGA (Magenta). The images are collected using Z stack mode of Polar-SIM. Two representative focal planes, one close to the bottom layer and one to the upper layer of the cell, are shown in the left with outlined regions enlarged. The 3D views of the regions (outlined) are enlarged on the right panel. Scale bars: 3 μm. Representative images of U2OS cells co-expressing mSc-PK1 and EGFP-Rab15 (**c**) or EGFP-Rab36 (**d**). Scale bars: 10 μm. All experiments in (**a**–**d**) were performed in triplicate with similar results. **e** Schematic image showing that PK1 promotes the formation of VANGL hexamer and assists plasma membrane docking of the Rab36-containing vesicles.

could potentially bind either three or six PK1 molecules. However, considering the size of the positively charged surface at the VANGL trimer-trimer interface, there is a substantial risk of steric clash if six PK1 molecules were to bind simultaneously in a 1:1 ratio. Furthermore, our SDS-PAGE result suggests that PK1-VANGL1 stoichiometric ratio is likely less than 1:1 (Supplementary Fig. 5a). Therefore, we hypothesize that the most probable stoichiometric ratio is three PK molecules per VANGL hexamer, which corresponds to a 1:2 ratio. It is also possible that the potential densities observed in the three symmetrical PK1 binding sites of VANGL could be misaligned when C1 symmetry was applied during refinement or could be enhanced due to the refinements conducted using C3 or D3 symmetries (Supplementary Fig. 6). This raises the alternative possibility that only one PK1 molecule binds to each VANGL hexamer, in a 1:6 ratio, as proposed by previous studies[58,59]. Nevertheless, further studies are necessary to clarify these possibilities.

The membrane tethering induced by the VANGL-PK1 complex shows good agreement with the VANGL hexamer structure. In this scenario, the two VANGL trimers are likely localized to the adjacent vesicular and plasma membranes, respectively. Through the formation of a stable hexamer with assistance from PK1, these trimers can pull the two membranes together (Fig. 5e). However, the vesicles have not fused with the cell membrane at this stage. They might be waiting for cues that trigger further action, such as calcium signaling. When the fusion is complete, VANGL will be presented at a specific membrane position and PCP will be gradually established. Additionally, because

https://doi.org/10.1038/s41467-024-55396-3

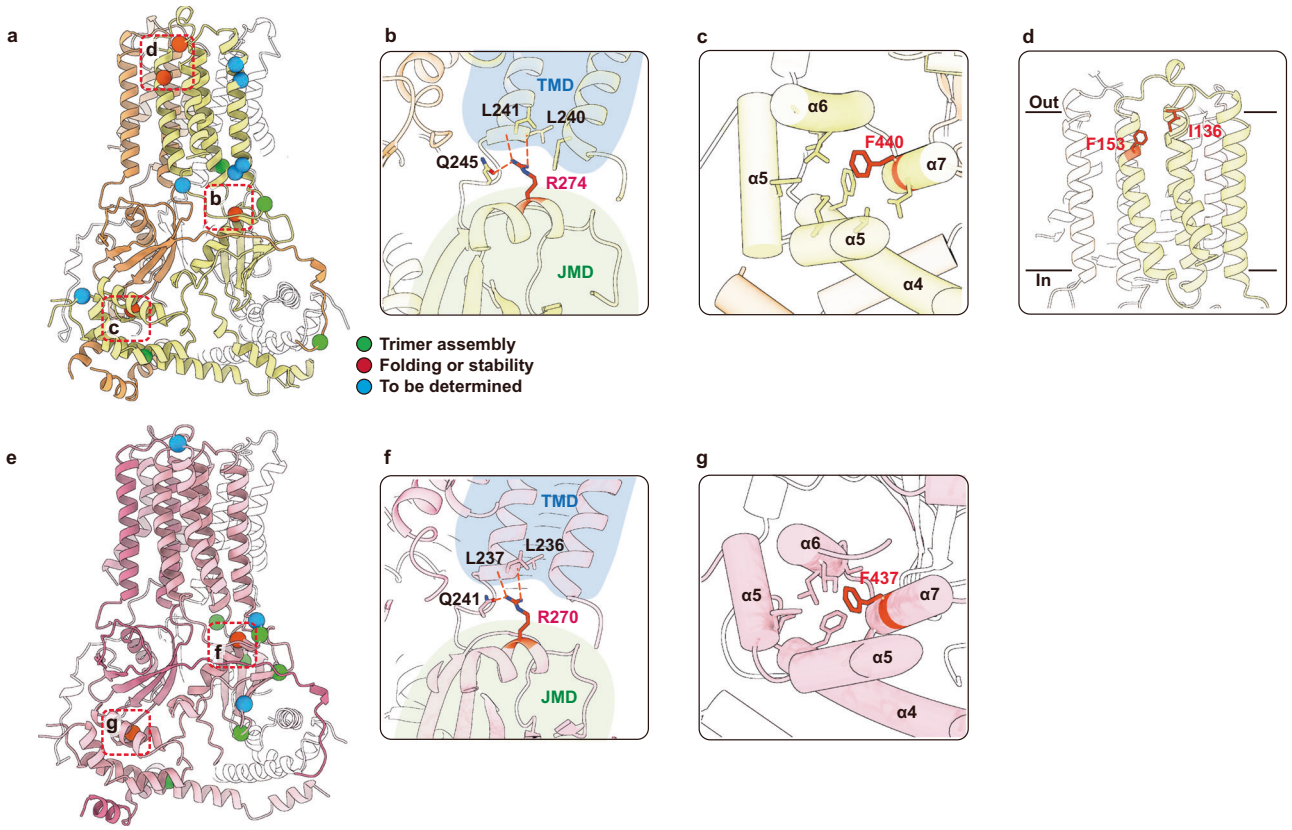

Fig. 6 | Mapping of the loss-of-function or disease-related mutations in VANGL proteins. a The disease-related mutations in VANGL1 structure. Mutations that localize at the trimer interface are colored in green. Mutations that may affect the folding and structural stability of individual VANGL subunit are colored in red. Other mutations are colored in blue. **b**–**d** Zoom-in views of several disease-related mutations. **e** The loss-of-function and disease-related mutations in VANGL2. The color code is the same as that in (**a**). **f**, **g** Zoom-in views of several disease-related mutations.

VANGL-containing vesicles in our experiment are concentrated at the peripheral side or leading edge of the cell membrane, they could directly replenish the membrane components or reorganize the local cell skeleton to further promote cell migration[6,60]. Intriguingly, the VANGL trimer structure indicates that the central pore surrounded by the three TMDs resembles a potential ion conduction pathway (Fig. 1f and Supplementary Fig. 3d). Thus, VANGL itself may serve as a channel to initiate signaling. However, the channel presumably only opens in response to certain stimuli. Nonetheless, further investigations are needed to ultimately elucidate the upstream and downstream signals within the VANGL-PK pathway.

Methods

Cell culture

HEK293S GnTI$^-$ cells (ATCC CRL-3022) were cultured at 37 °C with 5% CO_2 in Freestyle 293 Expression Medium (Gibco) supplemented with 1% Antibiotic-Antimycotic (Meilunbio) and 1% fetal bovine serum (VisTech). U2OS (ATCC HTB-96) cells were cultured at 37 °C with 5% CO_2 in Dulbecco's Modified Eagle Medium (DMEM, CellMax) supplemented with 10% fetal bovine serum (FBS, CellMax). Insect (Sf9) cells (ATCC CRL-1711) were cultured in Sf-900 II SFM medium (Gibco) at 28 °C. All cells were purchased from ATCC.

Expression and purification of VANGL1, VANGL2, and VANGL1-PK1 complex

DNA sequence of human VANGL1 or VANGL2 was cloned into pEG BacMan expression vectors with a green fluorescent protein (GFP) tag attached to the N-terminus. The sequence of human PK1 was cloned into another vector carrying an mCherry tag at the N-terminus and an MBP tag at the C-terminus to improve its solubility. These plasmids were transformed into DH10Bac *E. coli* cells for bacmid generation, and then the recombinant baculoviruses were produced in Sf9 cells using HighGene transfection reagent (ABclonal).

For the expression of VANGL1 and VANGL2, HEK293S GnTI$^-$ suspension cells at a density of 3×10^6 cells/ml were infected with 10% passage 3 viruses of VANGL1 or VANGL2 and cultured at 37 °C for 8–12 h. Then, the cells were transferred to 30 °C for 48 h with addition of 10 mM sodium butyrate. The cells were harvested by centrifugation at 6810 × *g* for 20 min, and frozen at −80 °C. The cell pellet was resuspended in Solubilization Buffer (50 mM HEPES pH 7.5, 500 mM NaCl, 15% glycerol, 1 mM DTT, 1 mM PMSF, 2 μg/ml DNase I, 4 mM ATP, 5 mM $MgCl_2$, and protease inhibitor cocktail (APExBIO)). After being dispersed by a hand-held homogenizer, cell membranes were solubilized with 2% (w/v) Lauryl maltose neopentyl glycol (LMNG, Anatrace) and 0.2% (wt/vol) Cholesteryl hemisuccinate (CHS, Anatrace) by gentle agitation for 3 h at 4 °C. The lysates were centrifugated at 38,900 × *g* for 40 min to remove the undissolved pellet and the supernatant was incubated with pre-equilibrated anti-GFP nanobody (GFPnb)-coupled NHS-activated beads (Smart-Lifesciences) at 4 °C for 2 h with gentle agitation. The beads were washed with 20 column volumes (CV) Wash Buffer (25 mM HEPES pH 7.5, 300 mM NaCl, 1 mM DTT, and 0.003% LMNG-0.0003% CHS) and then GST-tagged PreScission protease was added to release the target proteins (1:5 w/w ratio) at 4 °C overnight. Next, the protease was removed by incubating with the glutathione beads (Smart-Lifesciences). After concentration, the proteins were further purified by size exclusion chromatography (SEC) on a Superose 6 Increase 10/300 GL column (GE Healthcare) equilibrated with Final Buffer (25 mM HEPES pH 7.5, 150 mM NaCl, 1 mM DTT, and 0.003%

LMNG-0.0003% CHS). The peak fractions were collected and concentrated with a 30 kDa cut-off centrifugal filter (Millipore) to around 3 mg/ml. The protein samples were stored at −80 °C for later use.

Expression and purification of the VANGL1-PK1 complex were similar as above. Briefly, HEK293S GnTI⁻ suspension cells were co-infected with 8% passage 3 viruses of VANGL1 and 2% passage 3 viruses of PK1. The Solubilization Buffer, Wash Buffer, and Final Buffer were all made with 300 mM NaCl, while the other components were the same. Protein samples from SEC peak fractions were concentrated to around 0.7 mg/ml and stored at −80 °C.

Expression and purification of PK1$^{745\text{-}790}$

PK1$^{745\text{-}790}$ with an N-terminal 2×strep + flag tag followed by a PreScission protease recognition site was expressed in Shuffle T7 *E.coli* using the pET-28a vector. Bacteria were grown in 3 L Luria-Bertani medium at 37 °C with 100 mg/l ampicillin. Protein expression was induced at an OD_{600} of 0.6–1.0 with 1 mM IPTG for 20 h at 18 °C. The cells were harvested by centrifugation at 12,100 × *g* for 15 min and frozen at −80 °C.

For the purification of PK1$^{745\text{-}790}$, cells were resuspended in Lysis Buffer (50 mM HEPES pH 7.5, 300 mM NaCl, 15% glycerol, 1 mM DTT, 1 mM PMSF, 2 μg/ml DNase I, and protease inhibitor cocktail (APExBIO)) and broken by sonication. The lysates were centrifugated at 38,900 × *g* for 40 min to remove the cell debris and the supernatants were mixed with streptactin beads (Smart-Lifesciences) at 4 °C for 2 h with gentle agitation. The beads were rinsed with 30 CV Buffer A (25 mM HEPES pH 7.5, 300 mM NaCl, and 1 mM DTT) and incubated with PreScission protease at 4 °C overnight. Then the protease was removed by binding glutathione beads. The eluted protein was further purified by SEC in Buffer B (25 mM HEPES pH 7.5, 150 mM NaCl, and 1 mM DTT) using a Superose 6 Increase 10/300 GL column (GE Healthcare). The peak fractions were concentrated with a 3 kDa cut-off centrifugal filter (Millipore) and stored at −80 °C.

Cryo-EM sample preparation and data collection

VANGL1, VANGL2, or VANGL1-PK1 complex protein was directly used to prepare the EM grids. For preparation of the VANGL1-PK1$^{745\text{-}790}$ or VANGL2-PK1$^{745\text{-}790}$ complex, purified VANGL1 or VANGL2 was mixed with PK1$^{745\text{-}790}$ at a molar ratio of 1:4 on ice for 1 h before freezing grids. The final molar concentrations were 21 μM for VANGL1 and 84 μM for PK1$^{745\text{-}790}$, respectively. Similarly, the concentrations for VANGL2 and PK1$^{745\text{-}790}$ were 24 μM and 96 μM, respectively. In all cases, 3 μl sample was loaded onto glow-discharged holey carbon grids (Quantifoil R1.2/1.3 Au300). The grids were blotted and flash-frozen in liquid ethane using Vitrobot (FEI) at 10 °C and 100% humidity and then stored in liquid nitrogen until further use.

For the VANGL1 dataset, micrographs were acquired via SerialEM[61] on a Talos Arctica microscope (FEI) operated at 200 kV with a Gatan K2 Summit direct electron detector. A calibrated magnification of ×36,000 was used for imaging, yielding a pixel size of 1.16 Å, with the defocus ranging from 1.0 to 1.8 μm. Each micrograph was exposed for 8 s in 40 frames under a dose rate of 10 e^-/pixel/s, resulting in a total dose of 60 $e^-/Å^2$. 1649 micrographs were collected.

For VANGL2, VANGL1-PK1, VANGL1-PK1$^{745\text{-}790}$, and VANGL2-PK1$^{745\text{-}790}$ datasets, micrographs were collected using a 300 kV Titan Krios microscope (FEI) with a Gatan K3 camera. All data were required in super-resolution mode at a magnification of ×81,000 using the EPU software (Thermo Fisher Scientific). The physical pixel size was 1.07 Å, and the defocus range was 1.0–1.8 μm. The exposure time for each micrograph was 3.2 s, dose fractionated into 40 frames with a dose rate of 21.47 e^-/pixel/s. The total exposure dose was about 60 $e^-/Å^2$. The numbers of micrographs collected for the VANGL2, VANGL1-PK1, VANGL1-PK1$^{745\text{-}790}$, and VANGL2-PK1$^{745\text{-}790}$ samples were 5726, 1017, 3256, and 2201, respectively. The data collection parameters are summarized in Supplementary Tables 1 and 2.

Data processing, model building, and refinement

For VANGL1, two datasets (831 and 818 micrographs, respectively) were collected. Movies were first processed in Relion 4.0[62] using the MotionCorr2 program[63]. Then all the micrographs were imported into cryoSPARC v.4.4.1[64] and calculated by Patch CTF. A blob picker with a diameter of 250 Å was used for initial particle picking and generation of the 2D templates. Subsequently, particles were picked out using these 2D templates as reference. After 2D classification, 160,538 and 131,195 high-quality particles from each dataset were selected. Particles from the first dataset were used for Ab-initio reconstitution. Then particles from two datasets were combined and 3D classified using heterogeneous refinement. 144,253 particles were kept for a new round of Ab-initio reconstitution. Subsequently, 54,018 particles were chosen for Non-Uniform (NU) refinement. The final map of VANGL1 hexamer was refined to 3.0 Å resolution with a D3 symmetry using the gold-standard FSC = 0.143 standard.

For the datasets of VANGL2, VANGL1-PK1, VANGL1-PK1$^{745\text{-}790}$, and VANGL2- PK1$^{75\text{-}790}$, all data processing steps were performed in cryoSPARC v.4.4.1. Movies were motion corrected using Patch Motion Correction program. The following processing workflows were similar to that of the VANGL1 dataset. The final resolutions of these maps were 2.9 Å, 2.6 Å, 2.2 Å, and 2.5 Å, respectively.

For model building, the AlphaFold-predicted model of VANGL1 or VANGL2[48] was fitted and adjusted into the corresponding cryo-EM maps using ChimeraX[65] and Coot[66]. Refinement of the structures in real space and the comprehensive cryo-EM structure validation were performed using PHENIX[67,68]. Local resolutions were estimated in cryoSPARC. All the structure figures were prepared using ChimeraX.

Analytical ultracentrifugation (AUC) analyses

All protein samples with 0.3-0.8 OD absorbance at 280 nm were prepared in the buffer containing 25 mM HEPES pH 7.5, 150 mM NaCl, and 0.003% LMNG-0.0003% CHS. The following experimental parameters were used: 65,520 g, scan count 800, wavelength 280 nm, frequency 30 s, data resolution 10 μm, min radius 5.8 cm, max radius 7.2 cm, 8 °C, and An50 Ti Rotor (Beckman Coulter). Data analysis was conducted with SEDFIT software[69].

Pull-down assays

The plasmids of GFP-VANGL and mCherry-PK1-MBP were co-transfected into HEK293S GnTI⁻ cells at a density of 2 × 10^6 cells/ml. Specifically, 30 μg of each plasmid was mixed with 180 μg PEI (BIOHUB) and incubated in 200 μl OPT-MEM (Gibco) medium at room temperature for 25 min before adding into 30 ml suspension cells. The cells were cultured at 37 °C for 8–12 h and then transferred to 30 °C for 48 h with addition of 10 mM sodium butyrate. Cells were harvested by centrifugation at 4283 × *g* for 5 min and solubilized with the buffer containing 50 mM HEPES pH 7.5, 300 mM NaCl, 15% glycerol, 1 mM DTT, 1 mM PMSF, 2 μg/ml DNase I, protease inhibitor cocktail, 2% LMNG, and 0.2% CHS at 4 °C for 3 h. The supernatants were separated by centrifugation at 21,130 × *g* for 1 h and incubated with anti-mCherry nanobody (mCherrynb)-coupled beads at 4 °C for 2 h. After washing three times with the Wash Buffer, the beads were added to the SDS loading buffer. The protein extracts were separated by sodium dodecyl sulfate (SDS)–polyacrylamide gel electrophoresis (PAGE) with 8% gel. The mCherry and GFP fluorescence signals were detected using the ChemiDoc MP Imaging System (BIO-RAD). To verify the protein expression level, 2 × 10^6 cells were lysed with RAPI lysis buffer (25 mM Tris-HCl pH 7.5, 150 mM NaCl, 1 mM EDTA, 1% NP-40, 0.1% SDS, and protease inhibitors) on ice for 1 h. After removing the cell debits by centrifugation at 15,000 × *g* for 40 min, the supernatant was mixed with loading buffer and applied for SDS–PAGE analysis. The fluorescence signal was detected using the ChemiDoc MP Imaging System.

The quantifications were processed using ImageJ. The fluorescence images were first separated into red and green channels.

Subsequently, the threshold value was fine-tuned to ensure the optimal image analysis. Then the GFP to mCherry intensity ratio was calculated for each experimental group, taking into account of the input values. Finally, all measurements were normalized relative to the VANGL(WT)-PK1(FL) control.

Plasmid construction and transfection for localization analyses

For mScarlet-PK1, mNeongreen-VANGL1, mNeongreen-VANGL2, mScarlet-Rab3A, they were obtained by cloning the corresponding transcripts into the pEGFP-C1 vector (clontech) with the EGFP switched to corresponding fluorescent proteins. PCRs were performed using 2× Phanta Flash Master Mix (Vazyme) and restriction enzymes were from Takara. For mScarlet-PK1$^{1\text{-}744}$, mNeongreen-VANGL1^{10mut} and mNeongreen-VANGL1$^{1\text{-}495}$, the corresponding regions were deleted by overlap PCR. The other Rab plasmids were kind gifts from Dr Liang Ge at Tsinghua University and Dr Qiming Sun at Zhejiang University. Plasmids were transfected using Avalanche-OMNI (EZ Bio-systems).

Immunofluorescence and imaging

Cells were fixed with 4% paraformaldehyde in PBS for 15 min at 37 °C. For staining of WGA, cells were incubated with WGA diluted in PBS for 1 h. For immunostaining, cells were permeabilized with 0.1% Triton X-100 in PBS at room temperature for 5 min and blocked with 5% BSA for 15 min. Then, cells were incubated with indicated antibodies overnight at 4 °C, washed 3 times with PBS and incubated with secondary antibodies for 1 h. Cells were washed 3 times with PBS. Coverslips were mounted on slides using Fluoromount-G (SouthernBiotech). Representative images were collected with LSM980 confocal microscope (Carl Zeiss) in Airyscan mode equipped with a 63 × 1.4 NA Plan-Apochromat oil objective (Carl Zeiss). Images were acquired using ZEN (Carl Zeiss) and processed with ZEN or Fiji (ImageJ). For Z-stack, the images were collected with Polar-SIM (Airy) and processed using Imaris (Oxford).

Quantification and statistical analysis

For immunofluorescence, the analyses of ratio of cell periphery/total intensity were conducted using Fiji (ImageJ). The outline of the cells is circled to determine the overall fluorescence intensity within a single cell, and it was enlarged by −5 microns to determine the perinuclear fluorescence intensity. Therefore, the fluorescence intensity around the plasma membrane of the cell is equal to the fluorescence intensity of the whole cell minus the perinuclear fluorescence intensity. Three independent experiments were performed, each time 30 cells were randomly selected for statistical analysis. The corresponding percentage values were calculated and their comparisons were performed using GraphPad Prism (version 8.4.3).

Reporting summary

Further information on research design is available in the Nature Portfolio Reporting Summary linked to this article.

Data availability

Cryo-EM density maps of VANGL1, VANGL2, VANGL1-PK1, VANGL1-PK1$^{745\text{-}790}$, and VANGL2-PK1$^{745\text{-}790}$ have been deposited in the Electron Microscopy Data Bank under the accession codes EMD-61545, EMD-61546, EMD-61547, EMD-61548, and EMD-61549. Their atomic coordinates have been deposited in the Protein Data Bank under accession codes 9JK6, 9JK7, 9JK8, 9JK9, and 9JKA. The previously published structure utilized for analysis in this study can be accessed in the Protein Data Bank under accession code 7CHQ. Source data are provided with this paper.

References

1. Adler, P. N. Planar signaling and morphogenesis in Drosophila. *Dev. Cell* **2**, 525–535 (2002).
2. Mlodzik, M. Planar cell polarization: do the same mechanisms regulate Drosophila tissue polarity and vertebrate gastrulation? *Trends Genet.* **18**, 564–571 (2002).
3. Zallen, J. A. Planar polarity and tissue morphogenesis. *Cell* **129**, 1051–1063 (2007).
4. Goodrich, L. V. & Strutt, D. Principles of planar polarity in animal development. *Development* **138**, 1877–1892 (2011).
5. Wallingford, J. B. Planar cell polarity and the developmental control of cell behavior in vertebrate embryos. *Annu. Rev. Cell Dev. Biol.* **28**, 627–653 (2012).
6. Davey, C. F. & Moens, C. B. Planar cell polarity in moving cells: think globally, act locally. *Development* **144**, 187–200 (2017).
7. Henderson, D. J., Long, D. A. & Dean, C. H. Planar cell polarity in organ formation. *Curr. Opin. Cell Biol.* **55**, 96–103 (2018).
8. Carvajal-Gonzalez, J. M., Mulero-Navarro, S. & Mlodzik, M. Centriole positioning in epithelial cells and its intimate relationship with planar cell polarity. *Bioessays* **38**, 1234–1245 (2016).
9. Butler, M. T. & Wallingford, J. B. Planar cell polarity in development and disease. *Nat. Rev. Mol. Cell Biol.* **18**, 375–388 (2017).
10. Bastock, R., Strutt, H. & Strutt, D. Strabismus is asymmetrically localised and binds to Prickle and Dishevelled during Drosophila planar polarity patterning. *Development* **130**, 3007–3014 (2003).
11. Humphries, A. C. et al. A Van Gogh/Vangl tyrosine phosphorylation switch regulates its interaction with core planar cell polarity factors prickle and dishevelled. *PLoS Genet.* **19**, e1010849 (2023).
12. Yang, Y. & Mlodzik, M. Wnt-Frizzled/planar cell polarity signaling: cellular orientation by facing the wind (Wnt). *Annu Rev. Cell Dev. Biol.* **31**, 623–646 (2015).
13. Gray, RyanS., Roszko, I. & Solnica-Krezel, L. Planar cell polarity: coordinating morphogenetic cell behaviors with embryonic polarity. *Dev. Cell* **21**, 120–133 (2011).
14. Devenport, D. The cell biology of planar cell polarity. *J. Cell Biol.* **207**, 171–179 (2014).
15. Le Grand, F., Jones, A. E., Seale, V., Scimè, A. & Rudnicki, M. A. Wnt7a activates the planar cell polarity pathway to drive the symmetric expansion of satellite stem cells. *Cell Stem Cell* **4**, 535–547 (2009).
16. Gao, B. et al. Wnt signaling gradients establish planar cell polarity by inducing Vangl2 phosphorylation through Ror2. *Dev. Cell* **20**, 163–176 (2011).
17. Gros, J., Serralbo, O. & Marcelle, C. WNT11 acts as a directional cue to organize the elongation of early muscle fibres. *Nature* **457**, 589–593 (2009).
18. Heisenberg, C. P. et al. Silberblick/Wnt11 mediates convergent extension movements during zebrafish gastrulation. *Nature* **405**, 76–81 (2000).
19. Kilian, B. et al. The role of Ppt/Wnt5 in regulating cell shape and movement during zebrafish gastrulation. *Mech. Dev.* **120**, 467–476 (2003).
20. Qian, D. et al. Wnt5a functions in planar cell polarity regulation in mice. *Dev. Biol.* **306**, 121–133 (2007).
21. Dabdoub, A. et al. Wnt signaling mediates reorientation of outer hair cell stereociliary bundles in the mammalian cochlea. *Development* **130**, 2375–2384 (2003).
22. Wu, J., Roman, A. C., Carvajal-Gonzalez, J. M. & Mlodzik, M. Wg and Wnt4 provide long-range directional input to planar cell polarity orientation in Drosophila. *Nat. Cell Biol.* **15**, 1045–1055 (2013).
23. Strutt, D. I., Weber, U. & Mlodzik, M. The role of RhoA in tissue polarity and Frizzled signalling. *Nature* **387**, 292–295 (1997).
24. Boutros, M., Paricio, N., Strutt, D. I. & Mlodzik, M. Dishevelled activates JNK and discriminates between JNK pathways in planar polarity and wingless signaling. *Cell* **94**, 109–118 (1998).
25. Fanto, M., Weber, U., Strutt, D. I. & Mlodzik, M. Nuclear signaling by Rac and Rho GTPases is required in the establishment of epithelial planar polarity in the Drosophila eye. *Curr. Biol.* **10**, 979–988 (2000).

26. Weber, U., Paricio, N. & Mlodzik, M. Jun mediates Frizzled-induced R3/R4 cell fate distinction and planar polarity determination in the Drosophila eye. *Development* **127**, 3619–3629 (2000).
27. Habas, R., Kato, Y. & He, X. Wnt/Frizzled activation of Rho regulates vertebrate gastrulation and requires a novel Formin homology protein Daam1. *Cell* **107**, 843–854 (2001).
28. Winter, C. G. et al. Drosophila Rho-associated kinase (Drok) links frizzled-mediated planar cell polarity signaling to the actin cytoskeleton. *Cell* **105**, 81–91 (2001).
29. Taylor, J., Abramova, N., Charlton, J. & Adler, P. N. Van Gogh: a new drosophila tissue polarity gene. *Genetics* **150**, 199–210 (1998).
30. Wolff, T. & Rubin, G. M. Strabismus, a novel gene that regulates tissue polarity and cell fate decisions in Drosophila. *Development* **125**, 1149–1159 (1998).
31. Goto, T. & Keller, R. The planar cell polarity gene strabismus regulates convergence and extension and neural fold closure in Xenopus. *Dev. Biol.* **247**, 165–181 (2002).
32. Park, M. & Moon, R. T. The planar cell-polarity gene stbm regulates cell behaviour and cell fate in vertebrate embryos. *Nat. Cell Biol.* **4**, 20–25 (2002).
33. Montcouquiol, M. et al. Identification of Vangl2 and Scrb1 as planar polarity genes in mammals. *Nature* **423**, 173–177 (2003).
34. Kibar, Z. et al. Ltap, a mammalian homolog of Drosophila Strabismus/Van Gogh, is altered in the mouse neural tube mutant Loop-tail. *Nat. Genet.* **28**, 251–255 (2001).
35. Torban, E. et al. Genetic interaction between members of the Vangl family causes neural tube defects in mice. *Proc. Natl Acad. Sci.* **105**, 3449–3454 (2008).
36. Kibar, Z. et al. Mutations in *VANGL1* associated with neural-tube defects. *N. Engl. J. Med.* **356**, 1432–1437 (2007).
37. Lei, Y.-P. et al. VANGL2 mutations in human cranial neural-tube defects. *N. Engl. J. Med.* **362**, 2232–2235 (2010).
38. Radaszkiewicz, K. A., Sulcova, M., Kohoutkova, E. & Harnos, J. The role of prickle proteins in vertebrate development and pathology. *Mol. Cell. Biochem.* https://doi.org/10.1007/s11010-023-04787-z (2023).
39. Kunimoto, K., Weiner, A. T., Axelrod, J. D. & Vladar, E. K. Distinct overlapping functions for Prickle1 and Prickle2 in the polarization of the airway epithelium. *Front. Cell Dev. Biol.* **10**, 976182 (2022).
40. Tree, D. R. P. et al. Prickle mediates feedback amplification to generate asymmetric planar cell polarity signaling. *Cell* **109**, 371–381 (2002).
41. Carreira-Barbosa, F. et al. Prickle 1 regulates cell movements during gastrulation and neuronal migration in zebrafish. *Development* **130**, 4037–4046 (2003).
42. Deans, M. R. et al. Asymmetric distribution of prickle-like 2 reveals an early underlying polarization of vestibular sensory epithelia in the inner ear. *J. Neurosci.* **27**, 3139–3147 (2007).
43. Gubb, D. et al. The balance between isoforms of the prickle LIM domain protein is critical for planar polarity in Drosophila imaginal discs. *Genes Dev.* **13**, 2315–2327 (1999).
44. Jenny, A., Darken, R. S., Wilson, P. A. & Mlodzik, M. Prickle and Strabismus form a functional complex to generate a correct axis during planar cell polarity signaling. *EMBO J.* **22**, 4409–4420 (2003).
45. Butler, M. T. & Wallingford, J. B. Control of vertebrate core PCP protein localization and dynamics by Prickle2. *Development*. https://doi.org/10.1242/dev.121384 (2015).
46. Lee, S. Y., Kim, G. E., Kim, Y. G. & Park, H. H. A 1.3 A high-resolution crystal structure of an anti-CRISPR protein, AcrI E2. *Biochem. Biophys. Res. Commun.* **533**, 751–757 (2020).
47. Holm, L., Laiho, A., Toronen, P. & Salgado, M. DALI shines a light on remote homologs: one hundred discoveries. *Protein Sci.* **32**, e4519 (2023).
48. Abramson, J. et al. Accurate structure prediction of biomolecular interactions with AlphaFold 3. *Nature* **630**, 493–500 (2024).
49. Cukierman, E., Pankov, R., Stevens, D. R. & Yamada, K. M. Taking cell-matrix adhesions to the third dimension. *Science* **294**, 1708–1712 (2001).
50. Zhanghao, K. et al. Super-resolution imaging of fluorescent dipoles via polarized structured illumination microscopy. *Nat. Commun.* **10**, 4694 (2019).
51. Homma, Y., Hiragi, S. & Fukuda, M. Rab family of small GTPases: an updated view on their regulation and functions. *FEBS J.* **288**, 36–55 (2021).
52. Kibar, Z. et al. Novel mutations inVANGL1in neural tube defects. *Hum. Mutat.* **30**, E706–E715 (2009).
53. Kibar, Z. et al. Contribution of VANGL2 mutations to isolated neural tube defects. *Clin. Genet.* **80**, 76–82 (2011).
54. Andersen, M. R. et al. Mutation of the planar cell polarity gene VANGL1 in adolescent idiopathic scoliosis. *Spine* **42**, E702–E707 (2017).
55. Das, G., Jenny, A., Klein, T. J., Eaton, S. & Mlodzik, M. Diego interacts with prickle and Strabismus/Van Gogh to localize planar cell polarity complexes. *Development* **131**, 4467–4476 (2004).
56. Daulat, A. M. et al. PRICKLE1 contributes to cancer cell dissemination through its interaction with mTORC2. *Dev. Cell* **37**, 311–325 (2016).
57. Feng, D. et al. Regulation of Wnt/PCP signaling through p97/VCP-KBTBD7–mediated Vangl ubiquitination and endoplasmic reticulum–associated degradation. *Sci. Adv.* **7**, eabg2099 (2021).
58. Strutt, H., Gamage, J. & Strutt, D. Robust asymmetric localization of planar polarity proteins is associated with organization into signalosome-like domains of variable stoichiometry. *Cell Rep.* **17**, 2660–2671 (2016).
59. Strutt, H., Gamage, J. & Strutt, D. Reciprocal action of Casein Kinase Iε on core planar polarity proteins regulates clustering and asymmetric localisation. *Elife* **8**, https://doi.org/10.7554/eLife.45107 (2019).
60. Cheong, S. S. et al. The planar polarity component VANGL2 is a key regulator of mechanosignaling. *Front. Cell Dev. Biol.* **8**, 577201 (2020).
61. Mastronarde, D. N. Automated electron microscope tomography using robust prediction of specimen movements. *J. Struct. Biol.* **152**, 36–51 (2005).
62. Fernandez-Leiro, R. & Scheres, S. H. W. A pipeline approach to single-particle processing in RELION. *Acta Crystallogr. D. Struct. Biol.* **73**, 496–502 (2017).
63. Zheng, S. Q. et al. MotionCor2: anisotropic correction of beam-induced motion for improved cryo-electron microscopy. *Nat. Methods* **14**, 331–332 (2017).
64. Punjani, A., Rubinstein, J. L., Fleet, D. J. & Brubaker, M. A. cryoSPARC: algorithms for rapid unsupervised cryo-EM structure determination. *Nat. Methods* **14**, 290–296 (2017).
65. Pettersen, E. F. et al. UCSF ChimeraX: structure visualization for researchers, educators, and developers. *Protein Sci.* **30**, 70–82 (2021).
66. Emsley, P., Lohkamp, B., Scott, W. G. & Cowtan, K. Features and development of Coot. *Acta Crystallogr. D. Biol. Crystallogr.* **66**, 486–501 (2010).
67. Afonine, P. V. et al. Real-space refinement in PHENIX for cryo-EM and crystallography. *Acta Crystallogr. D. Struct. Biol.* **74**, 531–544 (2018).
68. Adams, P. D. et al. PHENIX: a comprehensive Python-based system for macromolecular structure solution. *Acta Crystallogr. D. Biol. Crystallogr.* **66**, 213–221 (2010).
69. Schuck, P. Size-distribution analysis of macromolecules by sedimentation velocity ultracentrifugation and lamm equation modeling. *Biophys. J.* **78**, 1606–1619 (2000).

Acknowledgements

We thank Dr. Liang Ge at Tsinghua University and Dr. Qiming Sun at Zhejiang University for sharing the Rab plasmids. We thank Jun Hu at the National Center for Protein Sciences at Peking University for assistance with drawing the model figure (Fig. 5e). We thank Dr Min Liu and Jing

Feng in Dr Alan Jian Zhu's laboratory at Peking University for helpful discussions. We thank the Cryo-EM platform and the School of Life Sciences of PKU for collecting cryo-electron microscopy data. We thank the Optical Imaging Core Facility of the National Center for Protein Sciences at Peking University for assistance with polar-SIM imaging. We thank the high-performance computing platform of Peking University for computational support. This research was funded by the National Key Research and Development Program of China (No. 2021YFA1302300 to Z.Z.) and the National Natural Science Foundation of China (No. 32171201 to Z.Z. and No. 32370732 to P.Z.). The study was also supported in part by the Center for Life Sciences (CLS), School of Life Sciences (SLS) of Peking University (to Z.Z. and P.Z.), the State Key Laboratory of Membrane Biology of China (to Z.Z.), the MOE Key Laboratory of Cell Proliferation and Differentiation of China (to P.Z.), and the Frontier Innovation Fund of Peking University Chengdu Academy for Advanced Interdisciplinary Biotechnologies (to Z.Z.).

Author contributions

Y.S. prepared protein samples, collected and processed cryo-EM data, and carried out the AUC and pull-down experiments. Z.Z. built and refined the structural models. S.J., Y.S., and P.Z. performed cell imaging experiments. J.T. contributed to analysis of the results. Z.Z. and P.Z. conceived and supervised the project. Z.Z. and P.Z. drafted the manuscript. All authors participated in revising the manuscript.

Competing interests

The authors declare no competing interests.

Additional information

Supplementary information The online version contains supplementary material available at https://doi.org/10.1038/s41467-024-55396-3.

Correspondence and requests for materials should be addressed to Pengli Zheng or Zhe Zhang.

Peer review information *Nature Communications* thanks Basavraj Khanppnavar and the other, anonymous, reviewer(s) for their contribution to the peer review of this work. A peer review file is available.